Zhao, D.; Chang, K.; Ebel, T.; Qian, M.; Willumeit, R.; Yan, M.; Pyczak, F.:

Microstructure and mechanical behavior of metal injection molded Ti–Nb binary alloys as biomedical material

In: Journal of the Mechanical Behavior of Biomedical Materials (2013)
Elsevier

DOI: 10.1016/j.jmbbm.2013.08.013

Microstructure and mechanical behavior of metal injection moulded Ti-Nb binary alloys as biomedical material

Dapeng Zhao [a,*], Keke Chang [b], Thomas Ebel [a], Ma Qian [c], Regine Willumeit [a], Ming Yan [c], Florian Pyczak [a]

[a] Helmholtz-Zentrum Geesthacht, Institute of Materials Research, Max-Planck-Str. 1, D-21502 Geesthacht, Germany

[b] RWTH Aachen University, Materials Chemistry, D-52056 Aachen, Germany

[c] The University of Queensland, School of Mechanical and Mining Engineering, ARC Centre of Excellence for Design in Light Metals, Brisbane, Qld 4072, Australia

*Corresponding author: Tel.: +49 (0)4152 871917; Fax: +49 (0)4152 871920.

E-mail address: Da-Peng.Zhao@hzg.de

Abstract:

The application of titanium (Ti) based biomedical materials which are widely used at present, such as commercially pure titanium (CP-Ti) and Ti-6Al-4V, are limited by the mismatch of Young's modulus between the implant and the bones, the high costs of products, and the difficulty of producing complex shapes of materials by conventional methods. Niobium (Nb) is a non-toxic element with strong β stabilizing effect in Ti alloys, which makes Ti-Nb based alloys attractive for implant application. Metal injection moulding (MIM) is a cost-efficient near-net shape process. Thus, it attracts growing interest for the processing of Ti and Ti alloys as biomaterial. In this investigation, metal injection moulding was applied to the fabrication of a series of Ti-Nb binary alloys with niobium content ranging from 10 wt.% to 22 wt.%, and CP-Ti for comparison. Specimens were characterized by melt extraction, optical microscopy, X-ray diffraction (XRD), scanning electron microscopy (SEM), energy-dispersive spectroscopy (EDS), and transmission electron microscopy (TEM). Titanium carbide formation was observed in all the as-sintered Ti-Nb binary alloys but not in the as-sintered CP-Ti. Selected area electron diffraction (SAED) patterns revealed that the carbides are Ti_2C. It was found that with increasing niobium content from 0 to 22%, the porosity increased from about 1.6 % to 5.8 %, and the carbide area fraction increased from 0 to about 1.8 % in the as-sintered samples. The effects of niobium content, porosity and titanium carbides on mechanical properties have been discussed. The as-sintered Ti-Nb specimens exhibited an excellent combination of high tensile strength and low Young's modulus, but relatively low ductility.

Keywords: Metal injection moulding; Ti-Nb alloy; Porosity; Titanium carbide; Tensile strength and Elongation; Young's modulus

1. Introduction

Titanium (Ti) and its alloys are fast emerging as the most attractive choice for the majority of medical applications. Commercially pure Ti (CP-Ti) has been an important biomaterial in this field for a long period, due to its high specific strength, excellent corrosion resistance and superior biocompatibility [1-4]. However, the mismatch in elastic modulus between CP-Ti (102~105 GPa) and the bone (4~30 GPa) may lead to the death of bone cells which is known as “stress shielding effect” [5]. As for Ti alloys, β-phase exhibits about 60~80 GPa of Young’s modulus, which is much lower than that of α-phase (100~120 GPa) [2, 6]. In addition, although some alloying elements such as V, Ni and Al are used to strengthen the Ti alloys, they lead to death of cells and long-term health problems [7, 8]. As a consequence, β- or near β-Ti alloys without cytotoxic element additions have been developed to overcome the above-mentioned limitations [9-13]. Niobium (Nb) is not only an important β-phase stabilizer, but also highly biocompatible. Furthermore, it is reported that Ti-Nb alloys have a lower elastic modulus compared with other binary Ti-based alloys [14]. They have thus attracted increasingly attention as promising implant materials.

The utilization of Ti alloys as implant material is limited because of the rather high costs of the raw material, the complex fabrication process, and associated geometry design constraints [15]. Metal injection moulding (MIM) could be an attractive choice to overcome these problems. One reason is that MIM can reduce costs due to its net-shape fabrication advantages, if high numbers of components are produced. On the other hand, MIM offers unique design flexibility that is not readily achievable with other fabrication processes [16-24]. This has been an important motivation for the fabrication of Ti and its alloys by MIM.

There have been several attempts in the MIM of Ti and Ti alloys in recent years.

CP-Ti components which had biocompatible properties were produced via MIM process. The debinding process was successfully controlled, so that the binder was completely removed before sintering. The tensile strength, elongation and oxygen levels of the components met the requirements for ASTM Grade 2 CP-Ti [25]. Obasi et al. [26] investigated the influence of processing parameters on mechanical properties of a Ti-6Al-4V alloy processed by MIM. A clear dependence of the tensile strength on the sintering temperature and time was observed. Moreover, it has been revealed that the heating rate during sintering, instead of the heating rate during thermo debinding, appears to be critical and has a significant influence on the final density and grain size. Recently, a Ti-17Nb binary alloy was first reported to be successfully fabricated by MIM [27]. In the following research, the microstructure and mechanical properties of this Ti-17Nb alloy was investigated [28]. The alloy showed a relative density of 94 % and a lamellar $\alpha + \beta$ Widmanstätten structure. The ultimate tensile strength of this alloy was about 770 MPa, which was much higher than that of hot-rolled Ti-17Nb (700 MPa). Moreover, the alloy exhibited a Young’s modulus of around 85 GPa, which was 20 GPa lower than that of CP-Ti Grade 2 according to AFTM F67.

In this study, the MIM technology was used to fabricate CP-Ti and Ti-Nb binary alloys containing (10~22) wt.% Nb. The purpose was to understand the effects of different Nb contents on the microstructure and mechanical properties of Ti-Nb binary alloys fabricated by MIM.

2. Experimental procedure

The Ti powder (< 45 μm) and Nb powder (< 110 μm) used in this study were supplied by TLS Technik GmbH, Germany, and MHC Industrial Corporation, China, respectively. Fig. 1 shows the morphology of the Ti and Nb powders.

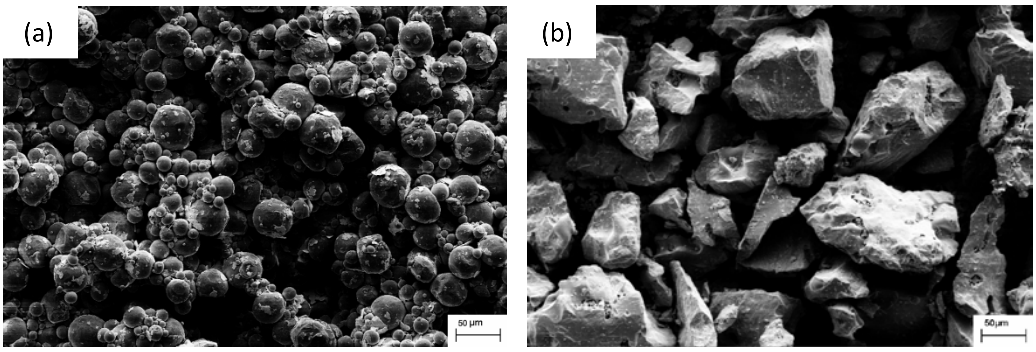

Fig. 1. Scanning electron micrograph of (a) Ti powder and (b) Nb powder.

Samples made from CP-Ti, Ti-10Nb, Ti-16Nb and Ti-22Nb (all wt.%) were produced by a MIM process, where the CP-Ti samples were fabricated as a reference.

The alloys were produced by blending elemental Ti powder and Nb powder. The powder blends were then mixed with a polymer binder that consists of 5 wt.% stearic acid, 35 wt.% polyethylene vinyl acetate and 60 wt.% paraffin wax in a Z-blade mixer at 120 °C for 2 h to form a batch of feedstock materials. All feedstock materials prepared had the same binder fraction of 31 vol.%.

After granulation, an Arburg 320S machine was used for the injection moulding of the feedstocks. The feedstocks were injection moulded as standard “dog bone” shape tensile specimens, with a nominal length of 89 mm and gauge thickness of 4.9 mm.

The green (after injection) samples were subjected to solvent extraction by immersing them into hexane at 40 °C for 20 h in a LÖMI EBA 50 debinding device. Thermal debinding and the sintering of specimens were conducted in a XERION XVAC 1600 furnace in one cycle under vacuum (10^{-3} Pa). The maximum sintering temperature was 1500 °C, and the holding time at the maximum temperature was 4 h to achieve a low porosity. The cooling rate was controlled to be 10 K/min. Several as-sintered CP-Ti, Ti-10Nb, Ti-16Nb and Ti-22Nb samples were treated by hot isostatic pressing (HIP) at 915 °C for 2 h under a pressure of 100 MPa. Besides the application in calculating the porosity of the as-sintered samples, the as-HIPed samples were also used for microstructure analyses and tensile tests to investigate the influence of porosity on mechanical properties of the Ti-Nb alloys.

The linear shrinkage of all samples after injection moulding and after sintering was found to be 11.5 ± 1 %. Fig. 2 shows a green sample and its as-sintered form. All the Ti-Nb alloys were made from elemental Ti powder and Nb powder. So it is more difficult to achieve a homogeneous structure than utilizing pre-alloyed powder. However, the as-sintered sample showed good shape retention without distortion compared to the green sample.

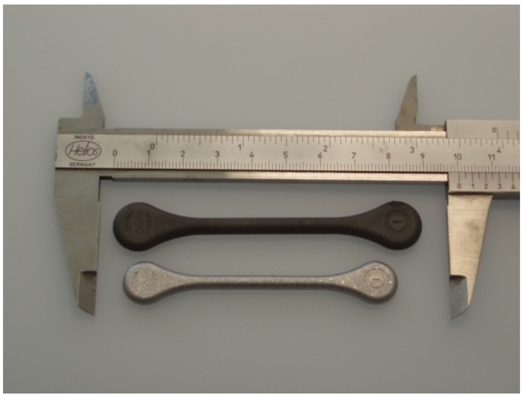

Fig. 2. Injection moulded and the as-sintered “dog-bone” tensile test specimens.

The density of the as-sintered samples and the as-HIPed samples were determined by the immersion method (Achimedes's principle) outlined in ASTM B311. A conventional LECO melt extraction system was used to determine the impurity levels of oxygen (O), carbon (C) and nitrogen (N). Constituent phases of the samples were characterized by X-ray diffraction (XRD), which was conducted on a conventional diffractometer using Cu K_α radiation. Optical microscopy (Olympus PMG3), scanning electron microscopy (SEM) (Zeiss-DSM962), energy-dispersive spectroscopy (EDS) in the SEM (EDAX LEO 1530) and transmission electron microscopy (TEM) (FEI Tecnai F20, operated at 200 kV) were used for microstructural examination and compositional analysis. Samples for optical microscopy and SEM were mechanically polished with SiO_2 pastes, cleaned in successive ultrasonic baths of ethanol, and then dried. TEM samples were prepared using a precision ion polishing system (PIPS) at -50 °C.

In order to understand the evolution of the carbide precipitates during sintering and to explain the differences in the microstructure of the as-sintered CP-Ti and Ti-Nb alloys, the solubility of carbon in Ti-10Nb and Ti-22Nb were calculated using Thermo-Calc software.

The as-sintered samples as well as the as-HIPed samples were directly used in the tensile tests without any preparation. Tensile tests were performed on a servohydraulic test machine equipped with a 100 kN load cell using a strain rate of 1.2×10^{-5} s^{-1} to measure tensile strength, elongation and Young's modulus. At least three samples of each configuration were tested.

3. Results and discussion

3.1 Impurity levels

Due to the influence of the impurity elements O, C and N on strength and ductility, the Ti powder, Nb powder and all the as-sintered samples described in the following sections were analyzed with respect to their content of these elements (Table 1). The deviation in these impurity levels of the as-sintered alloys was not significant. The oxygen and carbon levels of the as-sintered CP-Ti were in the range for CP-Ti Grade 2 according to ASTM F67. Since there is no standard available for MIM Ti-Nb alloys, ASTM F67 (Grade 2) for CP-Ti and ASTM F2885-11 for Ti-6Al-4V were used to compare the impurity levels of the Ti-Nb alloys. The as-sintered Ti-10Nb alloy exhibited carbon and oxygen levels within the requirement of both standards. Concerning Ti-16Nb and Ti-22Nb, both carbon and oxygen contents were acceptable as well. Moreover, the oxygen equivalent was calculated by O_{eq} = O + 2N +0.75 C (all wt.%) [29] for each composition. Since no data about O_{eq} of MIM Ti-Nb alloys is available in previous investigations, the results regarding MIM Ti-6Al-4V [30] were applied for comparison. The oxygen equivalents of all the as-sintered alloys were in the range of 0.33~0.41 wt.%, which were found to be lower than the critical value above which the ductility decreases dramatically. These results indicate that the impurity levels might not be a significant concern when comparing the mechanical properties of the samples in the present investigation.

Table 1 Impurity levels of the powders and the as-sintered samples (wt.%).

	O	C	N
Ti powder	0.0744	0.00469	0.0375
Nb powder	0.221	0.0152	0.0890
CP-Ti	0.175	0.0503	0.0628
Ti-10Nb	0.203	0.0562	0.0678
Ti-16Nb	0.255	0.0600	0.0525
Ti-22Nb	0.225	0.0589	0.0547

3.2 XRD study

Fig. 3 shows the XRD spectra of the as-sintered CP-Ti and Ti-Nb alloys. All the as-sintered Ti-Nb alloys were composed of α-phase and β-phase, while only α-phase was found in the as-sintered CP-Ti. The intensity of β-phase peaks gradually increased with higher Nb content, indicating an increase of β-phase fraction.

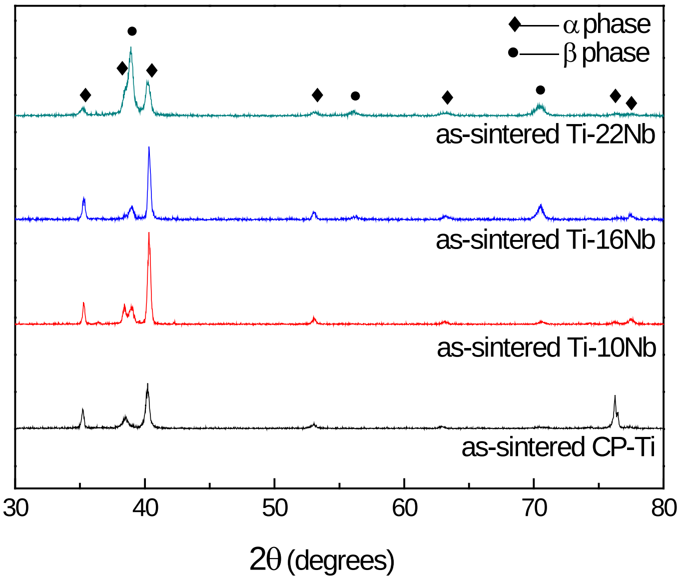

Fig. 3. XRD results for the as-sintered CP-Ti and Ti-Nb alloys.

3.3 Microstructure

The optical micrographs of the as-sintered CP-Ti and Ti-Nb binary alloys and the as-HIPed Ti-22Nb are shown in Fig. 4. The as-sintered CP-Ti showed the lowest porosity among the as-sintered samples and no precipitates. Furthermore, the pores are round and unconnected. However, in the as-sintered Ti-Nb alloys, apart from the presence of pores with sizes of 10~40 μm, fine acicular precipitates were observed, albeit only α-phase and β-phase were found by the XRD measurements. Such precipitates were also observed in the pore-free as-HIPed Ti-22Nb as presented in Fig. 4(e).

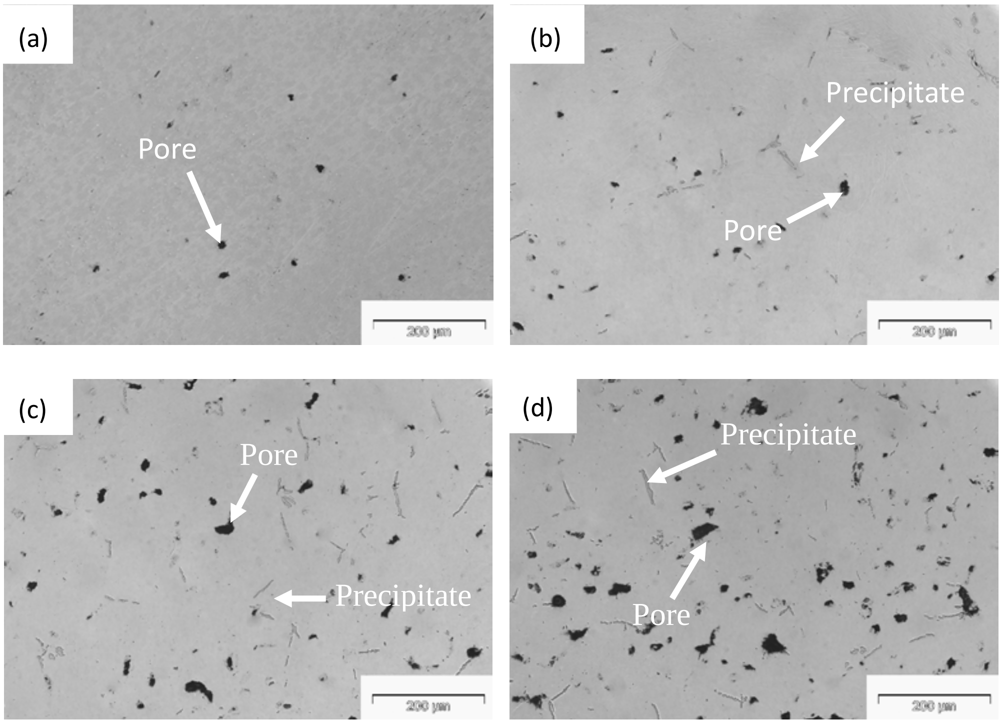

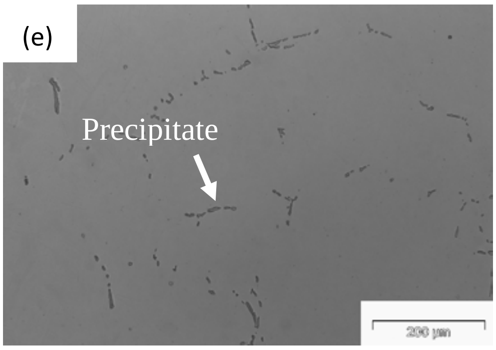

Fig. 4. Optical micrographs of (a) the as-sintered CP-Ti; (b) the as-sintered Ti-10Nb; (c) the as-sintered Ti-16Nb; (d) the as-sintered Ti-22Nb; (e) the as-HIPed Ti-22Nb.

Fig. 5 shows the back-scattered electron (BSE) and secondary electron (SE) SEM micrographs of the as-sintered Ti-10Nb, Ti-16Nb and Ti-22Nb. As presented in Fig. 5(a), 5(b) and 5(c), the as-sintered Ti-Nb alloys mainly consisted of α + β Widmanstätten structures with similar grain sizes of about 100~300 μm. The long strip shaped precipitates were observed in addition to the round pores. Most precipitates were distributed along grain boundaries (GBs). Albeit the grain sizes were not significantly different, an increased Nb content resulted in more refined α + β lamellas, an effect especially pronounced in the Ti-22Nb alloy (take note of higher magnification of Fig. 5(f) compared to Fig. 5(d) and 5(e)). As revealed by the SE-SEM micrographs – Fig. 5(d), 5(e) and 5(f) – the long strip precipitates were composed from particles which varied between 5 μm to 30 μm in size.

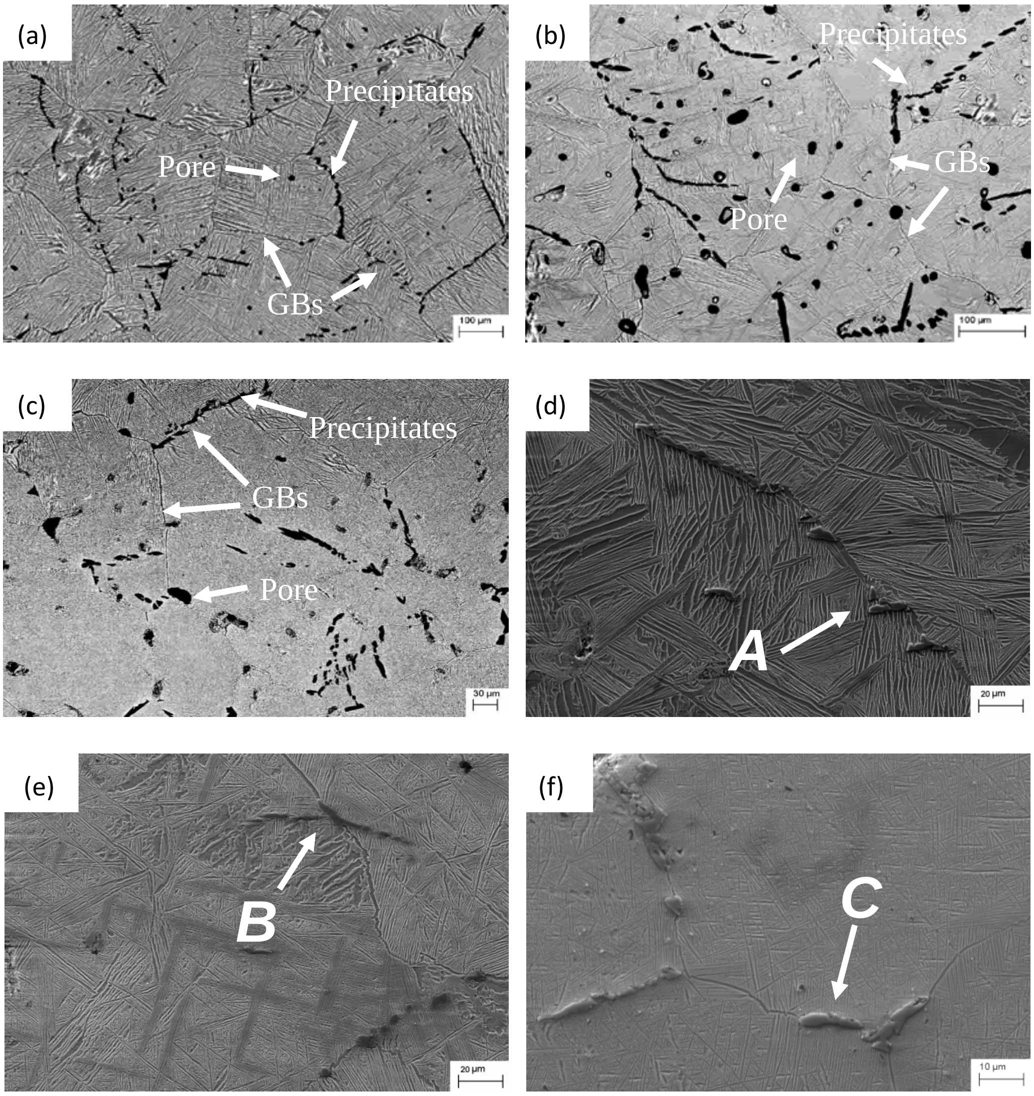

Fig. 5. SEM micrographs of the as-sintered Ti-Nb alloys: (a) Ti-10Nb (BSE-SEM image), (b) Ti-16Nb (BSE-SEM image), (c) Ti-22Nb (BSE-SEM image), (d) Ti-10Nb (SE-SEM image), (e) Ti-16Nb (SE-SEM image) and (f) Ti-22Nb (SE-SEM image) (Point ***A***, ***B*** and ***C*** are the precipitates in the as-sintered Ti-Nb alloys)

EDS results of the precipitates marked in Fig. 5 are presented in Table 2. The long strip shaped precipitates were identified to be titanium carbides (TiC_x). No dependence of morphology and composition of the TiC_x particles on Nb content was found. However, it is not possible to determine the exact stoichiometry just by EDS results because of its inaccuracy in carbon content analysis.

Table 2 EDS analyses of the precipitates in Fig. 5 (at.%).

	C	Nb	Ti
Point ***A*** in Fig. 5(d)	43.37	2.22	55.60
Point ***B*** in Fig. 5(e)	40.90	1.99	57.10
Point ***C*** in Fig. 5(f)	43.04	1.80	55.16

In order to investigate the nature of the TiC_x precipitates observed in the Ti-Nb alloys, the TiC_x precipitates were characterized by SAED (Selected Area Electron Diffraction) in the TEM. Respective bright field TEM micrographs and SAED patterns of the as-sintered Ti-22Nb are presented in Fig. 6. In Fig. 6(a), the TiC_x precipitate is surrounded by the matrix. Fig. 6(b), 6(c), 6(d) and 6(e) display the SAED patterns from the TiC_x precipitate. The TiC_x exhibits a face-centered cubic (FCC) structure with a lattice parameter of $\boldsymbol{a}$ = 4.3 Å. Between the main diffraction spots of the TiC_x precipitate, extra diffraction maxima at different zone axes with much lower intensity, i.e. ${}^{1}\!/_{2}(11\bar{1})$ and ${}^{1}\!/_{2}(3\bar{1}3)$, were observed, particularly at the [011] and [112] zone axes as presented in Fig. 6(b) and 6(e). In addition, it is important to note that the presence of {100} reflections from [011] zone axis as shown in Fig. 6(b) might attribute to double diffraction. These results indicate that the TiC_x precipitate may have a long-range-order structure with superlattice diffraction patterns.

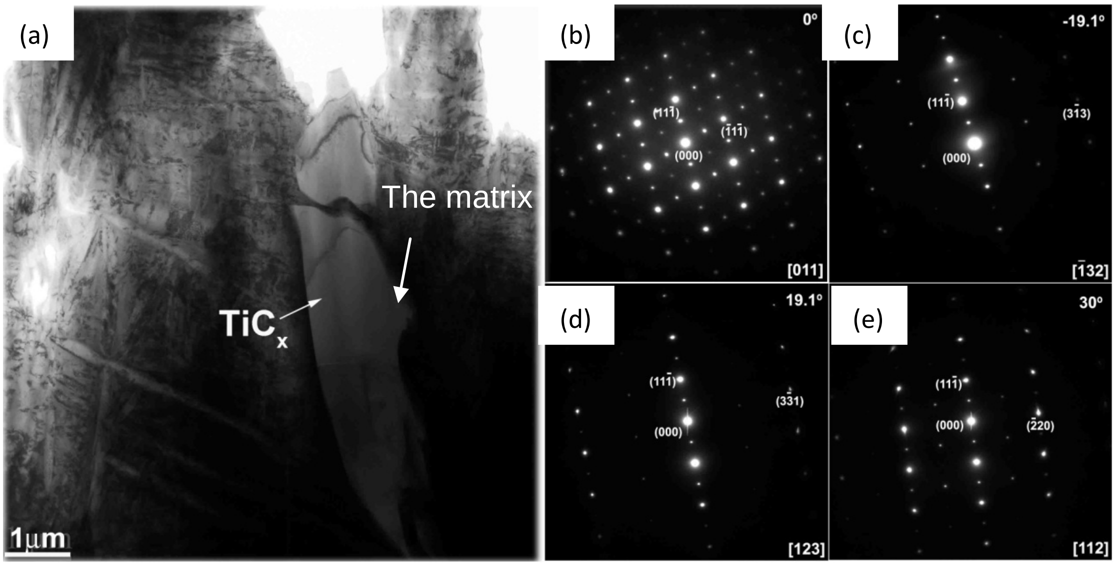

Fig. 6. TEM micrograph and SAED patterns of the as-sintered Ti-22Nb (a) the bright field image, (b) a SAED pattern showing TiC$_x$ reflections from [011], (c) a SAED pattern showing TiC$_x$ reflections from $[\bar{1}32]$ by tilting -19.1° away from [011], (d) a SAED pattern showing TiC$_x$ reflections from [123] by tilting 19.1° away from [011], (e) a SAED pattern showing TiC$_x$ reflections from [112] by tilting 30° away from [011].

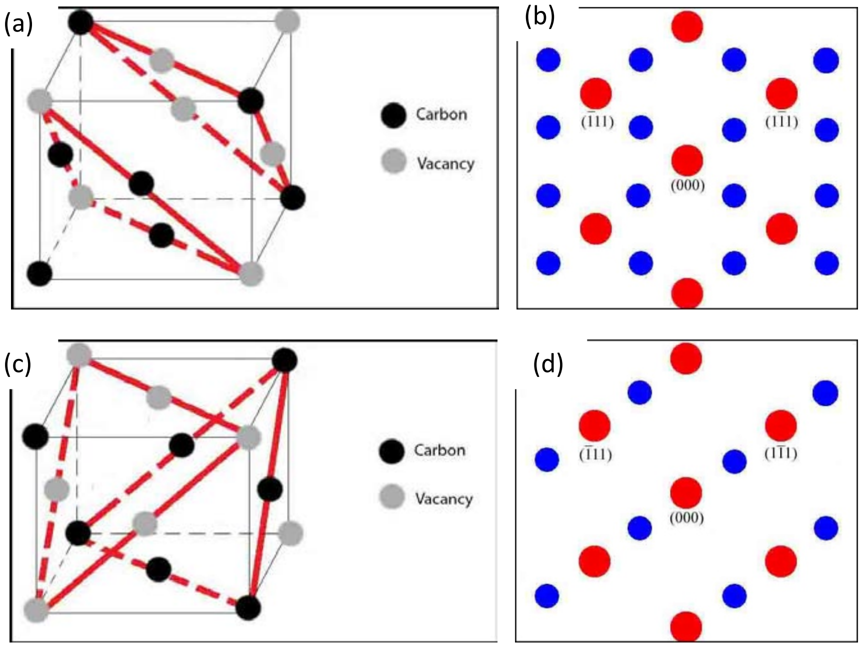

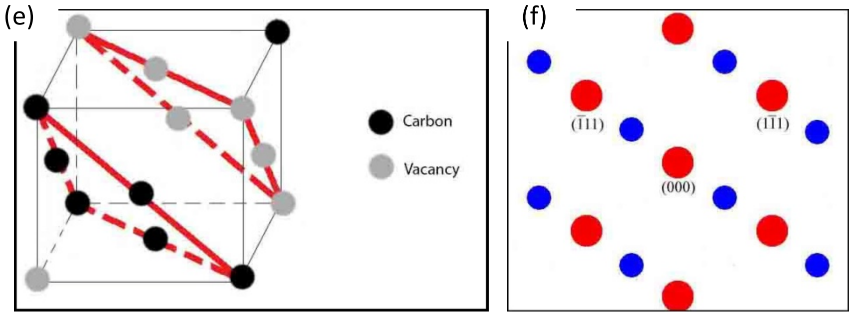

Fig. 7. Crystal structures and corresponding SAED patterns of *Fd3m*-Ti_2C and $R\bar{3}m$-Ti_2C (Ti atoms are invisible).

(a, b) *Fd3m*-Ti_2C; (c, d) $R\bar{3}m$-Ti_2C, type I; (e, f) $R\bar{3}m$-Ti_2C, type II.

Stoichiometric TiC adopts the cubic sodium chloride (NaCl) structure (*Fm3m* with a lattice parameter $\boldsymbol{a} \approx 4.33$ Å) [31]. Nonetheless, the titanium carbide usually exists in a substoichiometric form with statistically distributed substitutional vacancies on the carbon sublattice sites [32, 33]. The titanium carbide remains stable in the NaCl structure over a broad composition range (TiC_x, $0.48 \leq x \leq 1.00$) [34]. In the work of Wanjara et al. [35], a complete transformation from TiC to Ti_2C was observed in Ti-6Al-4V composites containing 20 vol.% of TiC particles sintered at 1500 °C for 0.5 h (measured at 1100 °C by reheating after sintering), nonetheless, only TiC was observed in the sample sintered at 1100 °C for 1h (measured at 1100 °C). Such a result indicates that, when sintering at 1500 °C, Ti_2C is more stable than TiC in Ti matrix, and Ti_2C can keep its structure afterwards even if at a lower temperature. Therefore, the TiC_x precipitates in the as-sintered Ti-Nb samples, which were sintered at 1500 °C for 4 h, might be Ti_2C instead of TiC. As revealed by previous investigators [35, 36], TiC and Ti_2C ($\boldsymbol{a} \approx 4.30$ Å) cannot be distinguished using optical or conventional scanning electron microscopy (using either secondary or backscattered electron imaging). However, Ti_2C particles usually exhibit a long-range-order superlattice structure, whereas TiC shows a typical FCC structure [37]. There are two types of Ti_2C, named as *Fd3m* and $R\overline{3}m$ structures [38]. Fig. 7 presents the schematic structure of both types of Ti_2C and corresponding diffraction patterns. Within the $R\overline{3}m$ space group, Ti_2C has two different crystal structures. It is difficult to distinguish *Fd3m*-Ti_2C and $R\overline{3}m$-Ti_2C by SAED patterns, because they can show the same diffraction pattern when many small variations are considered. In preceding papers [39, 40], *Fd3m*-Ti_2C were found to be more stable at lower temperature because the formation of $R\overline{3}m$-Ti_2C from disordered TiC_x or from ordered *Fd3m*-Ti_2C is kinetically hindered. Thus, considering the low cooling rate of the sintering process in this investigation, it is reasonable to assume that the precipitate in the as-sintered Ti-22Nb sample exhibits a *Fd3m* crystal structure. Besides, the presence of {100} reflections from [011] zone axis is consistent with the *Fd3m* space group. Consequently, the TiC_x precipitate investigated in the present work was determined as *Fd3m*-Ti_2C.

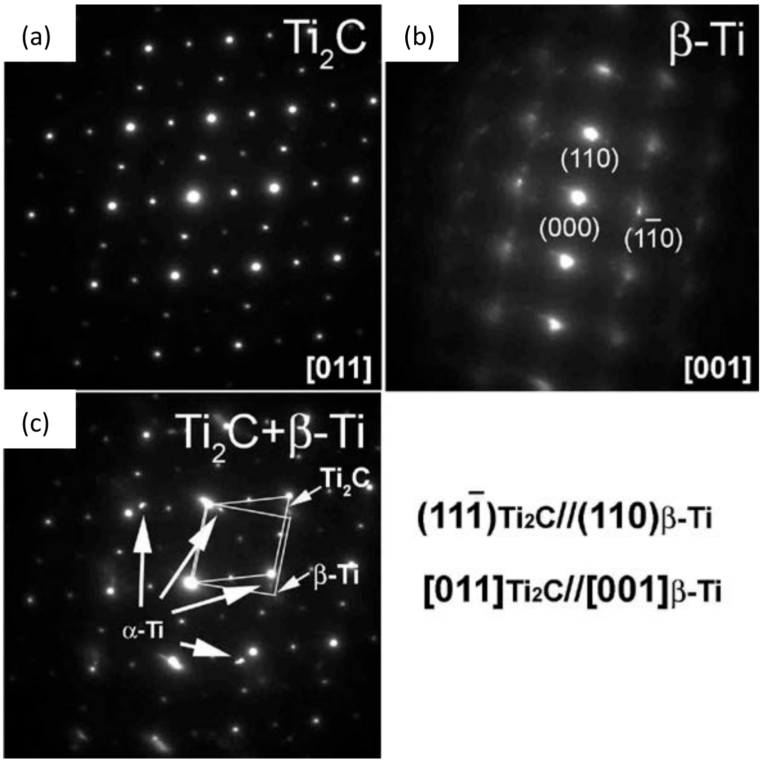

Fig. 8. SAED patterns of the Ti$_2$C precipitate in Fig. 6(a) and its surrounding matrix.

(a) a SAED pattern showing Ti$_2$C reflections from [011]; (b) a SAED pattern showing reflections of the matrix around the Ti$_2$C precipitate. The pattern was found to be β-Ti reflections from [001]; (c) a SAED pattern showing both Ti$_2$C and β-Ti reflections as well as several diffraction spots from α-Ti.

Fig. 8 presents the SAED patterns showing both the Ti$_2$C precipitate and the matrix around it. As revealed in Fig. 8(c), a clear crystallographic relationship between the Ti$_2$C precipitate and its surrounding β-Ti was found. Interestingly, the reflections from hexagonal close-packed (HCP) α-Ti were also observed, although only β-Ti was found around the Ti$_2$C precipitate in Fig. 8(b).

Sekimoto et al. [41] noticed that in a single-phase β-Ti matrix, little amount of *Fd3m*-Ti$_2$C particles was transformed to α-Ti. The transformation from Ti$_2$C into α-Ti occurs when a (111) plane of the *Fd3m*-Ti$_2$C slides and becomes one (0001) plane of α-Ti, then the stacking sequences is transformed from the ABCABC type in the former case to ABAB type in the latter. Fig. 9 displays the schematic diagram showing the relationship between atomic planes of α-Ti and *Fd3m*-Ti_2C, which can be given as: $(11\bar{1})_{Ti_2C} // (0001)_{\alpha-Ti}$.

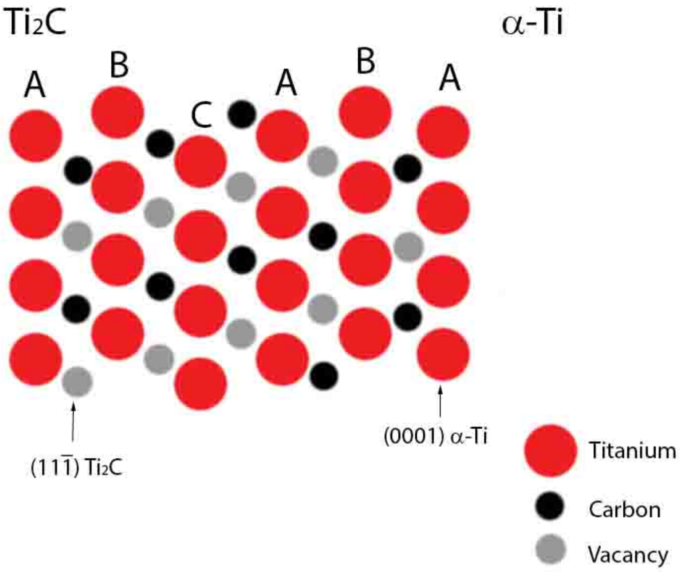

Fig. 9. Atomic planes of *Fd3m*-Ti_2C and α-Ti along $[11\bar{1}]$ direction of Ti_2C.

The bulk density of CP-Ti, Ti-10Nb, Ti-16Nb and Ti-22Nb alloy without pores were determined to be 4.501 g/cm^3, 4.792 g/cm^3, 4.924 g/cm^3 and 5.080 g/cm^3, respectively, after measuring samples exposed to an additional HIP process following the MIM production. Therefore, the porosity of the as-sintered samples could be measured by using:

$$Porosity = (1 - \rho_S / \rho_H) \times 100\% \quad (1)$$

where ρ_S is apparent density of the as-sintered samples and ρ_H is the apparent bulk density of the as-HIPed samples with the same composition.

The porosity and carbide area fractions in the as-sintered CP-Ti and Ti-Nb alloys and the as-HIPed Ti-22Nb alloy are presented in Fig. 10. For the as-sintered samples, both increased noticeably with increasing Nb content. It is important to note that the carbide area fraction of the as-sintered CP-Ti was zero.

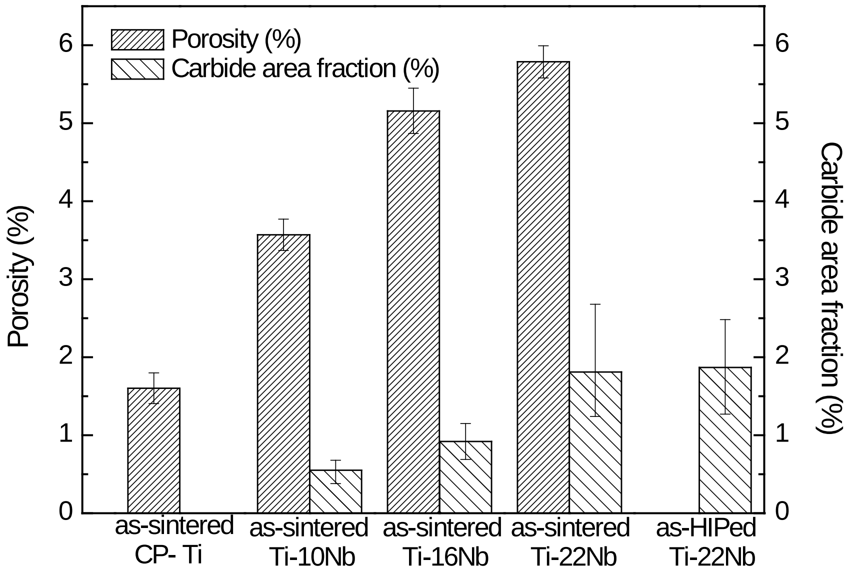

Fig. 10. Porosity and carbide area fraction in the as-sintered and the as-HIPed alloys.

The dependence of porosity on Nb content may be attributed to two main factors: one is the larger average particle size of the Nb powder compared with the Ti powder; and the other is the difficulty of Nb to dissolve by diffusion of Nb atoms into the matrix. During sintering, the contribution of surface diffusion and grain boundary diffusion increases with decreasing powder size [16]. In addition, finer powder particles can exhibit faster neck growth. Hence, they need less sintering time or a lower sintering temperature to achieve an equivalent degree of densification. Therefore, the highest relative density of an as-sintered sample for otherwise equal sintering conditions (temperature and time) should correlate with the highest content of small powders. In this case, since the average size of Nb powder was much larger than that of Ti powder, it is reasonable that a higher degree of porosity correlated with a higher Nb content. Secondly, Nakajima et al. [42] pointed out that from 800 °C to 1600 °C, the diffusion coefficient of Nb (about 5×10^{-12} m^2 s^{-1} at 1500 °C) is always lower than that of Ti (about 1×10^{-11} m^2 s^{-1} at 1500 °C) in the β-Ti matrix. Furthermore, the large average particle size of Nb powder leads to a long diffusion distance for Nb atoms to dissolve into the matrix, which enhances the diffusion difficulty. Therefore, the increasing porosity of the as-sintered samples with more Nb addition may be an effect of the higher content of coarse powder particles with increasing Nb content in combination with the rather slow diffusion of Nb atoms in a Ti matrix.

The observed precipitation of Ti_2C particles in Ti-Nb alloys was unexpected. Although carbon contents of the as-sintered Ti-Nb alloys were almost the same as that of the as-sintered CP-Ti, precipitates were only found in Ti-Nb alloys. To better understand the mechanisms of carbon solubility changes in Ti-Nb binary alloys, the pseudo-binary phase diagram of Ti-10Nb-C and Ti-22Nb-C were calculated using the Thermo-Calc software as shown in Fig. 11. The solubility of carbon in α-phase and β-phase could be predicted with the underlying CALPHAD (CALculation of PHAse Diagram) approach. In this work, we applied the thermodynamic parameters of the C-Nb-Ti system reported by Lee et al. [43] for the calculation.

Fig. 11 suggests that the addition of Nb reduces the α - β phase transformation temperature and leads to a decrease of carbon solubility in the matrix. It is reasonable to have a lower α - β phase transformation temperature in the alloy with higher Nb content, because Nb is a β-stabilizing element. As shown in Fig. 11, with increasing temperature, the solubility of carbon in Ti-10Nb and Ti-22Nb increases, reaching a maximum of 0.161 wt.% at 723 °C and 0.089 wt.% at 641 °C, respectively. At higher temperatures, the solubility of carbon decreases to 0.051 wt.% at 812 °C for Ti-10Nb and to 0.021 wt.% at 735 °C for Ti-22Nb. However, as the temperature further increases, the solubility of carbon increases with increasing temperature, reaching 0.307 wt.% in Ti-10Nb and 0.251 wt.% in Ti-22Nb at the sintering temperature of 1500 °C. Since the total carbon contents in the as-sintered Ti-Nb binary alloys were about 0.05~0.06 wt.%, all the carbon should be in solid solution as interstitial atoms and thus no titanium carbides should form at 1500 °C. During cooling, the precipitation of carbides will start below 1000 °C. Therefore, there was almost no grain growth inhibition effect by titanium carbides in the as-sintered Ti-10Nb, Ti-16Nb and Ti-22Nb alloys, where their grain sizes were all greater than 100 μm.

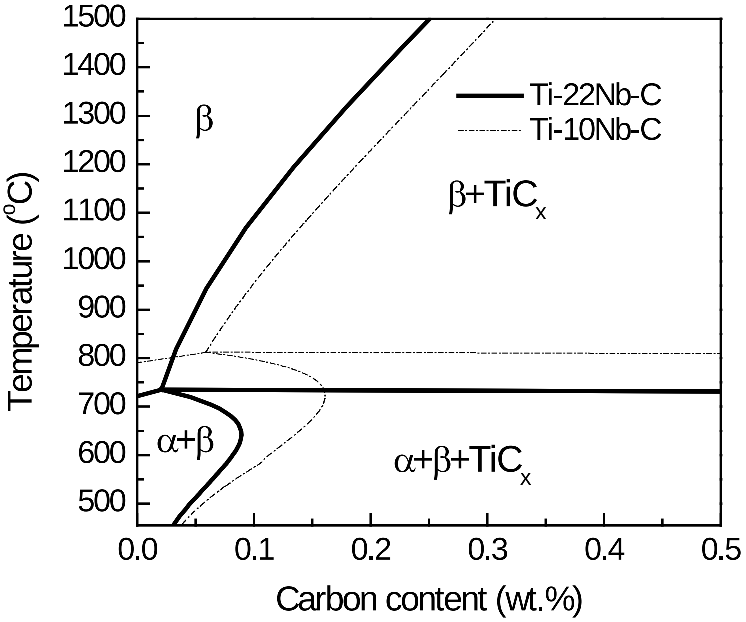

Fig. 11. The phase diagram of pseudo-binary Ti-10Nb-C and Ti-22Nb-C predicted using Thermo-Calc software.

3.4 Mechanical properties

The tensile properties of the as-sintered and the as-HIPed alloys are summarized in Table 3. The as-sintered alloys with a higher Nb content exhibited less elongation and lower Young's modulus but higher strength. The same trends of the strength vs. Nb content, elongation vs. Nb content and Young's modulus vs. Nb content were also observed in the as-HIPed samples. In general, the as-HIPed samples showed a higher strength and Young's modulus but similar elongation compared with the corresponding as-sintered alloys, whereas the elongation of the as-HIPed CP-Ti was about 40% higher than that of the as-sintered CP-Ti.

Table 3 Tensile properties of the as-sintered and the as-HIPed samples.

Composition	Yield Strength / MPa	Ultimate Tensile Strength / MPa	Elongation / %	Young’s Modulus / GPa
as-sintered CP-Ti	435 ± 10	531 ± 14	17.2 ± 3.0	112 ± 2.0
as-sintered Ti-10Nb	552 ± 19	638 ± 12	10.5 ± 1.9	85.2 ± 9.0
as-sintered Ti-16Nb	589 ± 20	687 ± 20	3.58 ± 0.61	78.4 ± 5.6
as-sintered Ti-22Nb	649 ± 31	754 ± 7.0	1.43 ± 0.51	70.9 ± 7.2
as-HIPed CP-Ti	525 ± 1.5	586 ± 1.0	24.2 ± 2.2	116 ± 2.3
as-HIPed Ti-10Nb	612 ± 3.6	708 ± 4.5	9.63 ± 1.1	90.1 ± 6.1
as-HIPed Ti-16Nb	661 ± 14	739 ± 27	4.96 ±0.31	82.2 ± 5.0
as-HIPed Ti-22Nb	687 ± 34	838 ± 14	1.30 ± 0.41	75.6 ± 7.6

To further understand the reasons for the differences in the mechanical properties of the as-sintered CP-Ti, Ti-10Nb, Ti-16Nb and Ti-22Nb alloys, the fracture surfaces of the failed tensile specimens are shown in Fig. 12. The fracture surface of the as-sintered CP-Ti tensile specimen showed a honeycomb structure, which is a typical feature of a ductile failure and means that the Ti powder bonding was metallurgically sound. All as-sintered Ti-Nb alloys exhibited a bimodal dimple structure. The size of “coarse dimples” of the Ti-Nb binary alloys was similar to the pore size in the alloys, and it is therefore assumed that these “coarse dimples” were pores lying now open on the fracture surface. The formation of “fine dimples” should correlate with the ductile deformation of the material between the pores. In Fig. 12(b), 12(c) and 12(d), particles were observed on the fracture surface of the as-sintered Ti-Nb alloys. EDS results revealed that the particles were Ti_2C.

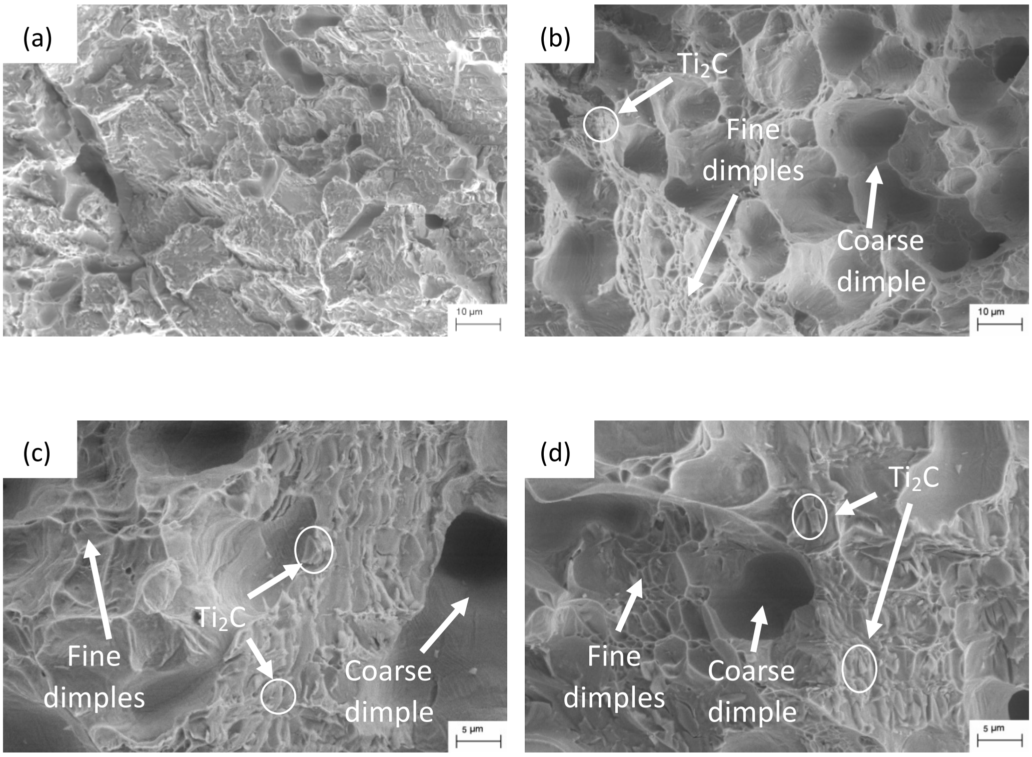

Fig. 12. The fracture surface of the as-sintered (a) CP-Ti, (b) Ti-10Nb, (c) Ti-16Nb and (d) Ti-22Nb, showing Ti_2C particles and dimples in all Ti-Nb binary alloys.

Based on the results shown above, it can be concluded that there are three factors determining the tensile properties of the as-sintered CP-Ti and Ti-Nb alloys.

The Nb content played a decisive role in reducing Young's modulus, and it also affected the tensile strength and elongation. Nb has a strong β-stabilizing effect on Ti alloys. So the decrease of Young's modulus with a higher amount of Nb addition in the as-HIPed alloys was expected. From an investigation which analyzed the influence of Nb addition on the mechanical properties of arc-melted Ti-Nb binary alloys [44], it is known that the tensile strength slightly increases from around 700 MPa to 750 MPa with Nb content ranging from 12 wt.% to 22 wt.%, but the elongation decreases from around 11 % to 9 % at the same time. However, in the present work, the differences in both tensile strength and elongation between the as-sintered Ti-Nb binary alloys were much larger. This suggests that the mechanical properties of the as-sintered Ti-Nb binary alloys have been affected by other factors.

The influence of porosity on the tensile properties is distinguishable by comparing the as-sintered and the as-HIPed samples. For instance, the Young’s modulus of the as-sintered Ti-22Nb was about 3 % to 6 % lower than that of the as-HIPed Ti-22Nb, which roughly correlates with the porosity of the as-sintered Ti-22Nb alloy. Accordingly, besides the influence of the Nb content, porosity has also played an appreciable role in determining the Young’s modulus of the as-sintered samples. As a result, even though the as-sintered Ti-10Nb, Ti-16Nb and Ti-22Nb alloys are α + β alloys, the specimens investigated here could exhibit comparable or lower Young’s modulus compared with some β-Ti alloys, such as Ti-12Mo-6Zr-2Fe and Ti-13Nb-13Zr with lower porosity [1]. Under monotonic tensile loading, the pores reduce the effective cross-section for load bearing and act as stress concentration sites, leading to strength and ductility decrease [45]. This explains why the tensile strength of the as-sintered samples was lower than that of as-HIPed samples. The elongation of the as-HIPed CP-Ti exhibited an increase of approximately 40 % compared to that of the as-sintered CP-Ti, which is in agreement with Bourcier finding [46] that even a porosity less than 5 % in CP-Ti can lead to a significant decrease of ductility. However, there was almost no influence of porosity on the ductility of the as-sintered Ti-Nb samples. The reason lies probably in the deterioration of the ductility caused by the Ti_2C precipitates, covering the effect of porosity.

Ti_2C precipitates enhanced the tensile strength but degraded the elongation of the as-sintered samples significantly. It has been shown that titanium carbides can increase the strength of Ti and its alloys through precipitation strengthening [47-49]. Fig. 11 predicts that a higher amount of carbides could be expected after sintering and cooling in the as-sintered Ti-Nb alloys with a higher Nb content. It should be noted that the tensile strength of the as-sintered Ti-22Nb is close to that of the arc-melted Ti-22Nb [44], although the former had a higher degree of porosity. This suggests that the positive contribution of the carbide precipitation had overcome the negative influence of porosity on tensile strength. Fig. 12(c) and 12(d) showed that in the as-sintered Ti-16Nb and Ti-22Nb, the Ti_2C particles are readily visible on the fracture surface by cleavage fracture. The low ductility of the as-sintered Ti-16Nb and Ti-22Nb alloys is thus attributed to the large amount of carbides. The influence of Ti_2C particles on Young's modulus is not clear yet and will be addressed in further investigation.

4. Summary

This study aimed at the understanding of the effects of different Nb contents on the microstructure and mechanical properties of Ti-Nb binary alloys. Ti and Ti-Nb alloys with a porosity of less than 5% have been produced via the MIM process, and the shape of tensile test specimens was well preserved from the green state to the as-sintered state.

Titanium carbides were found in the as-sintered Ti-Nb alloys by optical microscopy.

Nevertheless, no obvious titanium carbide peaks were detected by the XRD measurements. TEM results revealed that the carbides were Fd3m-Ti_2C particles. The α-Ti which might be transformed from Ti_2C was observed by SAED. The relationship between atomic planes of α-Ti and Fd3m-Ti_2C was given as: $(11\bar{1})_{Ti_2C}//(0001)_{\alpha-Ti}$.

The increase of Nb content led to an increase of porosity and Ti_2C formation. The increased formation of Ti_2C is due to the decrease of carbon solubility with increasing Nb content which promotes carbide precipitation. The increased porosity arises from the increased use of coarse Nb powder and the slow diffusion of Nb both decelerating the sintering process resulting in higher porosity.

The addition of Nb lowered Young's modulus and elongation but increased the strength. The Nb content, porosity and titanium carbides are the main factors to influence the mechanical properties. The higher Nb content and higher porosity resulted in a lower Young's modulus. The increase of strength was observed in both the as-sintered and the as-HIPed samples with increasing Nb content. This should correlate with not only the higher Nb content, but also the higher amount of carbide precipitates. Such a combined effect overcompensated the negative influence of porosity on the strength in the as-sintered Ti-Nb alloys. A distinct relationship between the Ti_2C precipitates and the low elongation of the as-sintered Ti-16Nb and Ti-22Nb was observed. The fractography revealed that the carbide particles were responsible for the low ductility. The as-HIPed Ti-Nb samples and the as-sintered Ti-Nb samples exhibited similar tensile ductility. However, it is unwarranted to claim that the porosity had almost no effect on the ductility of the as-sintered Ti-Nb alloy, because the influence of porosity on the ductility might have been masked by the more significant influence of Ti_2C precipitates on the ductility.

In summary, the Ti-Nb alloys fabricated by MIM showed a good combination of high strength and low Young's modulus. It is thus feasible to use MIM to fabricate Ti-Nb alloys with excellent strength and low Young's modulus by low amount of alloying elements addition. However, the unexpected precipitation of titanium carbides should be controlled to improve the ductility.

Acknowledgement

This research was funded by Helmholtz – CSC Fellowship Programme. The authors are grateful to Uwe Lorenz, Wolfgang Limberg, Andreas Dobernowsky, Petra Fischer, Michael Oehring, Jonathan Paul, Martin Wolff and Juliano Soyama from Helmholtz-Zentrum Geesthacht.

References

[1] M. Geetha, A.K. Singh, R. Asokamani, A.K. Gogia, Prog. Mater. Sci., 54 (2009) 397-425.

[2] M. Niinomi, Mater. Sci. Eng. A, 243 (1998) 231-236.

[3] A. Biesiekierski, J. Wang, M. Abdel-Hady Gepreel, C. Wen, Acta Biomater., 8 (2012) 1661-1669.

[4] E. Bertrand, T. Gloriant, D.M. Gordin, E. Vasilescu, P. Drob, C. Vasilescu, S.I. Drob, J. Mech. Behav. Biomed. Mater., 3 (2010) 559-564.

[5] M. Long, H.J. Rack, Biomaterials, 19 (1998) 1621-1639.

[6] M. Niinomi, Metall. Mater. Trans. A, 33A (2002) 477-486.

[7] Q. Wei, L. Wang, Y. Fu, J. Qin, W. Lu, D. Zhang, Mater. Design, 32 (2011) 2934-2939.

[8] D. Starosvetsky, I. Gotman, Biomaterials, 22 (2001) 1853-1859.

[9] A. Ramarolahy, P. Castany, F. Prima, P. Laheurte, I. Péron, T. Gloriant, J. Mech. Behav. Biomed. Mater., 9 (2012) 83-90.

[10] R. Banerjee, S. Nag, H.L. Fraser, Mater. Sci. Eng. C, 25 (2005) 282-289.

[11] G. He, M. Hagiwara, Mater. Sci. Eng. C, 26 (2006) 14-19.

[12] M. Abdel-Hady, K. Hinoshita, M. Morinaga, Scripta Mater., 55 (2006) 477-480.

[13] D. Kuroda, M. Niinomi, M. Morinaga, Y. Kato, T. Yashiro, Mater. Sci. Eng. A, 243 (1998) 244-249.

[14] M. Tane, T. Nakano, S. Kuramoto, M. Hara, M. Niinomi, N. Takesue, T. Yano, H. Nakajima, Acta Mater., 59 (2011) 6975-6988.

[15] L. Bolzoni, E.M. Ruiz-Navas, E. Neubauer, E. Gordo, J. Mech. Behav. Biomed. Mater., 9 (2012) 91-99.

[16] R.M. German, Powder Injection Molding, First ed., Metal Powder Industries Federation New York, 1990.

[17] D. Whittaker, Powder Inject. Mould. Int., 1 (2007) 27-32.

[18] R.M. German, Powder Inject. Mould. Int., 3 (2009) 21-37.

[19] E. Baril, Powder Inject. Mould. Int., 4 (2010) 22-32.

[20] T. Ebel, Powder Inject. Mould. Int., 2 (2008) 21-30.

[21] D. Whittaker, Powder Inject. Mould. Int., 5 (2011) 47-53.

[22] F.H. Fores, Powder Metall. Met. C+, 45 (2007) 303-310.

[23] R.M. German, Int. J. Powder Metall., 46 (2010) 11-17.

[24] J.A. Sago, M.W. Broadley, J.K. Eckert, Int. J. Powder Metall., 48 (2012) 41-49.

[25] A.T. Sidambe, I.A. Figueroa, H.G.C. Hamilton, I. Todd, J. Mater. Process. Tech., 212 (2012) 1591-1597.

[26] G.C. Obasi, O.M. Ferri, T. Ebel, R. Bormann, Mater. Sci. Eng. A, 527 (2010) 3929-3935.

[27] J.-E. Bidaux, C. Closuit, M. Rodriguez-Arbaizar, E. Carreno-Morelli, European Cells and Materials, 22 (2011) 32.

[28] J.-E. Bidaux, C. Closuit, M. Rodriguez-Arbaizar, D. Zufferey, E. Carreño-Morelli, Powder Inject. Mould. Int., 6 (2012) 72-75.

[29] H. Conrad, Acta Metall., 14 (1966) 1631-1633.

[30] T. Ebel, O.M. Ferri, W. Limberg, F.P. Schimansky, Advances in Powder Metallurgy & Particulate Materials-2011, Metal Powder Industries Federation, San Francisco, 2011.

[31] D.A. Aksyonov, A.G. Lipnitskii, Y.R. Kolobov, Comp. Mater. Sci., 65 (2012) 434-441.

[32] R. Eibler, J. Phys.-Condes. Matter, 19 (2007) 22.

[33] A.I. Gusev, Usp. Fiz. Nauk, 170 (2000) 3-40.

[34] K.E. Tan, A.M. Bratkovsky, R.M. Harris, A.P. Horsfield, D. Nguyen-Manh, D.G. Pettifor, A.P. Sutton, Model. Simul. Mater. Sc., 5 (1997) 187-198.
[35] P. Wanjara, R.A.L. Drew, J. Root, S. Yue, Acta Mater., 48 (2000) 1443-1450.
[36] V.N. Lipatnikov, L.V. Zueva, A.I. Gusev, A. Kottar, Phys. Status Solidi, 40 (1998) 1211-1218.
[37] D.G. Konitzer, M.H. Loretto, Acta Metall., 37 (1989) 397-406.
[38] R. Eibler, J. Phys. - Condens. Mat., 14 (2002) 4425-4444.
[39] M.Y. Tashmetov, V.T. Em, C.H. Lee, H.S. Shim, Y.N. Choi, J.S. Lee, Physica B, 311 (2002) 318-325.
[40] V.T. Em, M.Y. Tashmetov, Phys. Status Solidi B-Basic Res., 198 (1996) 571-575.
[41] W. Sekimoto, H. Tsuda, S. Mori, Mater. Trans., 53 (2012) 1405-1411
[42] H. Nakajima, M. Koiwa, ISIJ Int., 31 (1991) 757-766.
[43] B.-J. Lee, Metall. Mater. Trans. A, 32A (2001) 2423-2439.
[44] Y.-H. Hon, J.-Y. Wang, Y.-N. Pan, Mater. Trans., 44 (2003) 2384-2390.
[45] O.M. Ferri, T. Ebel, R. Bormann, Mater. Sci. Eng. A, 527 (2010) 1800-1805.
[46] R.J. Bourcier, D.A. Koss, R.E. Smelser, O. Richmond, Acta Metall., 34 (1986) 2443-2453.
[47] B.-Y. Chen, K.-S. Hwang, Mater. Sci. Eng. A, 541 (2012) 88-97.
[48] Z.Q. Chen, D. Hu, M.H. Loretto, X. Wu, Mater. Sci. Tech., 20 (2004) 343-349.
[49] H.W. Wang, J.Q. Qi, C.M. Zou, D.D. Zhu, Z.J. Wei, Mater. Sci. Eng. A, 545 (2012) 209-213.